quantum beam science

MDPI

Article

The Magnetic Phase Transition and Universality Class of *h*-$YMnO_3$ and *h*-$(Y_{0.98}Eu_{0.02})MnO_3$ Under Zero and Applied Pressure

Sonja Holm-Dahlin [1,2,*], Sofie Janas [1], Andreas Kreisel [3], Ekaterina Pomjakushina [4], Jonathan S. White [2], Amy L. Fennell [4] and Kim Lefmann [1]

1 Nanoscience Center, Niels Bohr Institute, University of Copenhagen, 2100 Copenhagen, Denmark; sofie.janas@gmail.com (S.J.); lefmann@nbi.ku.dk (K.L.)
2 Laboratory for Neutron Scattering and Imaging, Paul Scherrer Institute, 5232 Villigen PSI, Switzerland; jonathan.white@psi.ch
3 Institut für Theoretische Physik, Universität Leipzig, 04103 Leipzig, Germany; kreisel@itp.uni-leipzig.de
4 Laboratory for Multiscale Materials Experiments, Paul Scherrer Institute, 5232 Villigen PSI, Switzerland; ekaterina.pomjakushina@psi.ch (E.P.); apoole969@gmail.com (A.L.F.)
* Correspondence: sonja@fys.ku.dk; Tel.: +45-28306064

Received: 30 June 2018; Accepted: 27 August 2018; Published: 31 August 2018

Abstract: We investigated the antiferromagnetic phase transition in the frustrated and multiferroic hexagonal manganites *h*-$YMnO_3$ (YMO) and *h*-$(Y_{0.98}Eu_{0.02})MnO_3$ (YEMO). Elastic neutron scattering was used to study, in detail, the phase transition in YMO and YEMO under zero pressure and in YMO under a hydrostatic pressure of 1.5 GPa. Under conditions of zero pressure, we found critical temperatures of $T_N = 71.3(1)$ K and 72.11(5) K and the critical exponent 0.22(2) and $\beta = 0.206(3)$, for YMO and YEMO, respectively. This is in agreement with earlier work by Roessli et al. Under an applied hydrostatic pressure of 1.5 GPa, the ordering temperature increased to $T_N = 75.2(5)$ K, in agreement with earlier reports, while β was unchanged. Inelastic neutron scattering was used to determine the size of the anisotropy spin wave gap close to the phase transition. From spin wave theory, the gap is expected to close with a critical exponent, β', identical to the order parameter β. Our results indicate that the gap in YEMO indeed closes at $T_N = 72.4(3)$ K with $\beta' = 0.24(2)$, while the in-pressure gap in YMO closes at 75.2(5) K with an exponent of $\beta' = 0.19(3)$. In addition, the low temperature anisotropy gap was found to have a slightly higher absolute value under pressure. The consistent values obtained for β in the two systems support the likelihood of a new universality class for triangular, frustrated antiferromagnets.

Keywords: critical exponent; multiferroics; spin-wave; magnetic phase transition; applied pressure; inelastic neutron scattering

1. Introduction

In multiferroic materials, the structural, magnetic, and electronic order parameters are intertwined. For this reason, multiferroic materials are relevant for applications in, for example, transducers, actuators, and multi-memory devices [1–3]. Practical applications of multiferroics require, in most cases, functionality at room temperature which has so far been discovered only in $BiFeO_3$ material. However, the study of multiferroicity at low temperatures should help to unravel the physical mechanism behind this phenomenon [4,5]. Multiferroics are, in general, divided into two classes: Type-I, where the ferroelectric transition takes place at higher temperatures than the magnetic ordering, and type-II where the two ordering phenomena occur at roughly the same temperature.

One common class of multiferroics is the hexagonal rare-earth manganites $R\mathrm{MnO_3}$. These compounds are type-I multiferroics for R, namely, Sc, Y, Ho Er, Tm, Yb and Lu [6,7]. The results presented in this paper concern the hexagonal magnanite h-$\mathrm{YMnO_3}$ (YMO), which has only one type of magnetic ion and is the most studied rare-earth manganite. Additionally to being multiferroic, YMO is also a frustrated antiferromagnet with spin-2 and a Curie–Weiss temperature of $\theta_{CW} = -500$ K [8]. The ferroelectric ordering in YMO takes place at 1258 K [9], while the magnetic ordering takes places at a much lower temperature of $T_N = 72$ K [8,10,11]. However, other authors have reported slightly different ordering temperatures: 70 K [12] and 75 K [13,14].

In this study, we were concerned with the nature of the magnetic phase transition in the hexagonal manganite spin system. In general, physical systems exhibiting a phase transition can be classified according to the values of their critical exponents. Systems sharing the same critical exponents behave identically to the phase transition, independent of the details of the model that describes their physics. For the triangular Heisenberg antiferromagnet, there are indications that frustration may lead to a separate universality class [15,16] which could pave the way to understanding differences in the appearing phases and the nature of phase transitions in such frustrated systems in general. Additionally, investigating the system under applied pressure allows us to probe the stability of the ordered phase and investigate how the critical exponent of the system evolves.

We have performed experiments on YMO under zero and high applied pressures. Some of our zero-pressure experiments, however, were performed on a Eu-doped sample, h-$(\mathrm{Y_{0.98}Eu_{0.02}})\mathrm{MnO_3}$ (YEMO). Initially, the doped sample was used inadvertently, as the low doping value made the YEMO sample indistinguishable from YMO, except by gamma spectroscopy. However, at this low doping rate, YEMO is expected to have magnetic properties very similar to YMO [17,18], and including the YEMO data in the present study serves to reconfirm these earlier findings. For YMO, it was earlier found by neutron diffraction with up to 6 GPa pressure that the applied pressure increases the ordering temperature by approximately 1 K/GPa [13,14], but reduces the average ordered moment [19].

Here, we investigate the critical exponent, β, in two different ways. Firstly, we use neutron diffraction to measure the magnetic ordered signal, and secondly, inelastic neutron scattering is used to observe the spin wave signal. Because of the large easy-plane anisotropy of the system [20], the spin wave is gapped, allowing it to be used for independent determination of critical parameters. We record the spin wave gap and the ordered magnetic moment as a function of temperature under zero pressure (YMO and YEMO) and under a hydrostatic pressure of 1.5 GPa (in YMO). We find that the Néel temperature in YMO increases from 71.3(1) K to 75.2(5) K with an applied pressure of 1.5 GPa and that the ordered moment is reduced. The critical exponent of the phase transition is very small, $\beta = 0.206(3)$, for the most accurate determination (YEMO). Both observations are in accordance with some of the earlier studies. When approaching the phase transition, the spin wave gap reduces from $\Delta = 2.15(1)$ meV at base temperature to zero at T_N with an apparent critical exponent of $\beta' = 0.24(2)$ which is consistent with the elastic data within one standard deviation. Under applied pressure, the spin wave gap also tracks the Néel temperature with a similar behaviour as in zero pressure.

In summary, we find similar critical behaviour for YMO and YEMO. In addition, we do not find any evidence that the critical behaviour changes upon application of pressure, that is, the system remains in the same universality class with a very small value of β, which could be a universality class that is specific to frustrated, triangular systems. The particular energies of the microscopic interactions are, however, affected by pressure, as observed in the increase of the ordering temperature and the value of the anisotropy gap.

2. Experimental Details

The crystal structures of h-$\mathrm{YMnO_3}$ and h-$\mathrm{Y_{0.98}Eu_{0.02}MnO_3}$ are hexagonal and both have lattice constants of $a = b = 6.108$ Å (measured in the current work) and $c = 11.39$ Å. The unit cell of h-$\mathrm{YMnO_3}$ is shown in Figure 1 along with the magnetic structure, which is a three-sublattice "120 degree structure" within the basal (a, b) planes and stacked along the c-direction. The precise magnetic ground state has

been a topic of some debate [21], but has been determined using both second-harmonic generation [22] and, most recently, inelastic neutron scattering [23] to be the P6′$_3$cm′ structure, as shown in Figure 1. For the YEMO sample, 2% of the yttrium spacers are replaced with europium, the spin of which is expected to be paramagnetic at the temperatures used in this work.

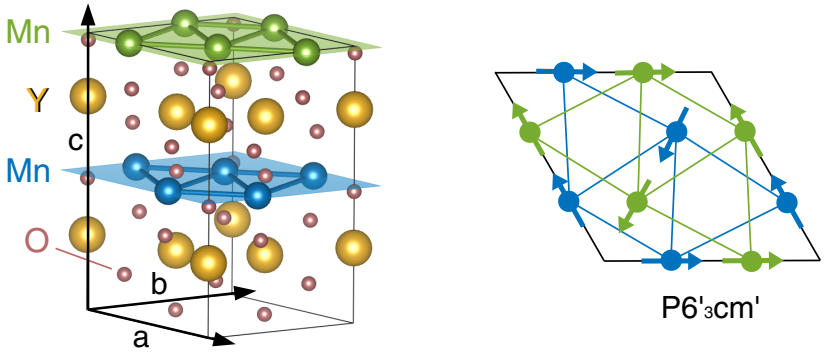

Figure 1. The left panel shows the unit cell of $YMnO_3$ (YMO) with the Mn layers highlighted with green and blue (drawn using Vesta [24]). On the right, the structure of the magnetic ground state, P6′$_3$cm′, is displayed. The 3D spin structure is projected on the (a, b) plane, and bonds symbolizing that the in-plane interactions in the two layers are coloured in blue and green (see Ref. [23]).

The single crystal samples used in the experiments were produced with the travelling solvent floating zone method [10]. The sample quality was assessed using X-ray and neutron Laue diffraction and neutron two-axis diffraction. The 2% europium doping content was confirmed with gamma spectroscopy. The lattice parameters obtained were consistent with the literature values for *h*-$YMnO_3$ for all sample pieces. Based on this, we consider the YEMO and YMO samples to be very similar. Each sample piece appeared to be of mostly good quality with a single phase with limited mosaicity of 1 degree at Full Width at Half Maximum (FWHM). Small, completely misaligned grains were found in the largest sample piece. These grains are, however, too small to contribute significantly to the neutron scattering signal.

For the experiments under zero pressure, a large sample rod of YEMO with a mass of 5.25 g was mounted with glue on an aluminium holder. For the pressure cell experiment, two smaller pieces of the YMO (370 mg and 232 mg) were co-aligned and mounted in a clamp pressure cell. The pressure transmitting medium was a 1:1 mix of Fluorinerts FC-75:FC-77. The applied pressure was monitored in-situ at low temperature by measuring the lattice compression of a small NaCl single crystal co-mounted with the sample, and using its reported equation of state [25]. During preparation, the two pieces of YMO became misaligned inside the cell. The experiment was therefore carried out using the data from only the larger piece, while the signal from the smaller, misaligned piece contributed only to the elastic and inelastic background. Data was taken from the same set-up under both zero and 1.5 GPa pressure. ILL-type Orange cryostatswere used in all experiments to control the temperatures of the samples.

Inelastic measurements were carried out at the cold-neutron triple-axis spectrometer (TAS) RITA-II at the Paul Scherrer Institute (PSI), lVilligen, Switzerland. The instrument was configured in the monochromatic imaging mode [26,27] with a constant final energy of 5.0 meV for the experiment without a pressure cell and 4.6 meV for the experiment with pressure, giving an energy resolution of 0.2–0.3 meV, depending on the energy transfer and resolution in the $\boldsymbol{q}$-space of 0.015 r.l.u. The incoming collimation was 80′ without the pressure cell and 40′ with the pressure cell. The imaging mode gave RITA-II a natural outgoing collimation of 40′. A Be-filter was placed on the outgoing side for both experiments to reduce the contamination from second-order neutrons.

Elastic measurements were carried out at RITA-II using two settings: the monochromatic three-axis imaging mode and the two-axis mode. Both set-ups had an incoming collimation of 80′ and

an outgoing Be-filter. Additional elastic measurements were done at the thermal TAS spectrometer EIGER, PSI using a final energy of 14.64 meV giving an energy resolution of 1 meV. A pyrolytic graphite filter was placed on the outgoing side to reduce contamination from second-order neutrons.

3. Experimental Results: Neutron Diffraction

In Figure 2, longitudinal scans of the $\boldsymbol{q} = (100)$ magnetic Bragg peak in YEMO and YMO are shown for a selection of temperatures near T_N. The signal from the peak was measured (**a**) in a standard Orange cryostat at zero pressure (YEMO) and (**b**) in the clamp cell under pressures of 0 GPa and 1.5 GPa (YMO; only high pressure data shown). Even with our relatively good $\boldsymbol{q}$-resolution, the expected Lorentzian broadening from short-range magnetic order [28] was not seen, even in the critical region just around T_N. For that reason, we fitted all data with single Gaussians. The found intensities are plotted as a function of temperature in Figure 3. All fitting parameters can be found in Figures A1 and A3 in the appendix.

At zero pressure (Figure 2a), the intensity of the magnetic Bragg peak in YEMO is seen to decrease as the temperature approaches T_N, but a clear signal lingers above T_N. Despite the lack of visible signal broadening, we attribute this to some type of critical scattering from the unordered phase, giving an overall shape of the intensity curve similar to that usually found around phase transitions [28]. In the longitudinal scans, a small shift in the peak position is visible. The shift indicates a change of 0.05% in the lattice parameters close to T_N.

The data in Figure 2b was obtained under an applied pressure of 1.5 GPa, and stems from sample rotation scans of the peak at $\boldsymbol{q} = (100)$, where the YMO sample is aligned in the (a, b) plane. Scans were made while both heating and cooling the sample slowly, though only the heating data is shown here. The data collected under zero pressure (not shown) is consistent with that collected under high pressure, with the modification that the ordering temperature was a few Kelvin lower here.

In order to ensure that the data obtained were independent of the experimental conditions, e.g., the energy resolution, the intensity of the magnetic Bragg peak at $\boldsymbol{q} = (100)$ in YEMO under zero pressure was measured as a function of temperature under three different experimental conditions: cold TAS (RITA-II), thermal TAS (EIGER), and cold two-axis (RITA-II without analyser). The peak intensities obtained in the three experiments are shown together in Figure 3a.

In the cold-neutron TAS experiment, longitudinal scans were performed for each temperature step and intensities were obtained by Gaussian fits in order to correct for minor changes in lattice parameters. In the two-axis (cold- and thermal-neutron) experiments, sample rotation scans in the (a, b) plane were performed and fitted (no raw data shown). In the two cold-neutron experiments, the samples were thermalized between measurements at each temperature. A simple scaling factor was used to present the results on a common intensity axis. In the thermal-neutron TAS experiment, the intensity was measured by standing on the peak centre and counting while heating the sample. The small shift in the peak position, observed in the cold-neutron TAS experiment, is much smaller than the instrument resolution of the thermal-neutron TAS, and the shift will therefore not influence the measurement of the intensity. To fit this data onto the common axis, the intensities were scaled and the temperature was shifted by 0.79 K to compensate for the temperature drag of the sample inside the cryostat.

The three measuring methods were found to give identical results in terms of curve shape, including the amount of critical scattering found around and above T_N. We aimed to obtain estimates of T_N and β by a power law ($I \propto (1 - T/T_N)^{2\beta}$) fit to the intensities in the critical region of the cold-neutron TAS intensities in Figure 3. Since the standard method of subtracting the critical scattering from short-range order [28] did not apply in the present case, we adopted a purely experimental-based method, in which we directly fitted the diffraction data from the long-range order in a region where the contamination from scattering above T_N was negligible. To identify the correct fitting range within the critical region as well as an approximate value of T_N, double logarithmic plots of the intensities versus the reduced temperature, $t = (T_N - T)/T_N$, were used for different values of T_N. The approximate value of T_N was then chosen as the one that would give the largest critical region (straight line in the

log-log plot (see appendix, Figure A2). The final power law fit was subsequently performed with both β and T_N as free parameters. The fitting region found was from 60 K to 71.5 K, corresponding to a reduced temperature range of $t = 0.012 - 0.17$. The fit yielded the values $T_N = 72.11(5)$ and $\beta = 0.206(3)$.

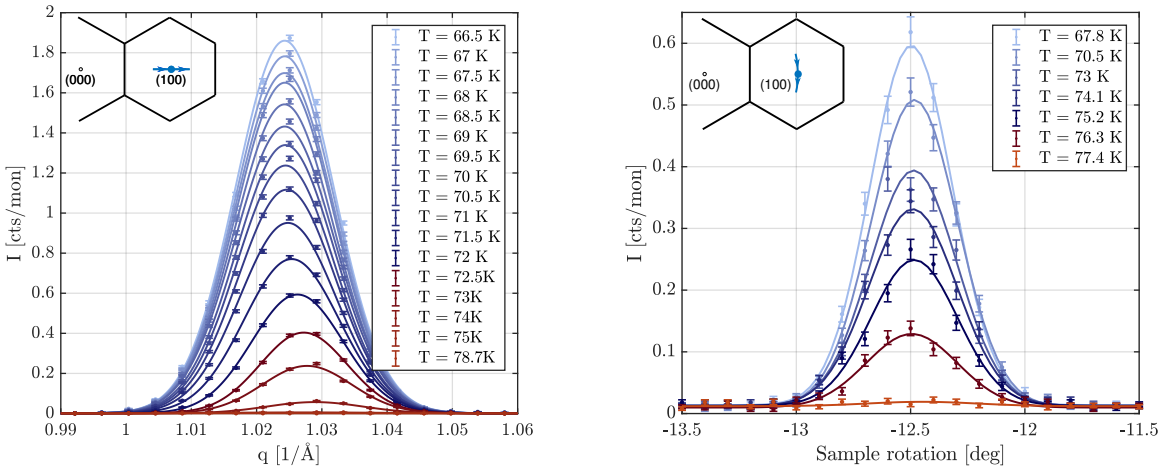

Figure 2. The magnetic Bragg peak at $\boldsymbol{q} = (hkl) = (100)$ measured at RITA-II in three-axis mode. The red and blue colours indicate scans were made above and below the critical temperatures respectively. (**a**) Longitudinal scans of h-$(Y_{0.98}Eu_{0.02})MnO_3$ (YEMO) made under zero pressure. The sample was thermalized between each scan; (**b**) Sample rotation scans of YMO made under 1.5 GPa pressure. The sample was heated slowly while scanning.

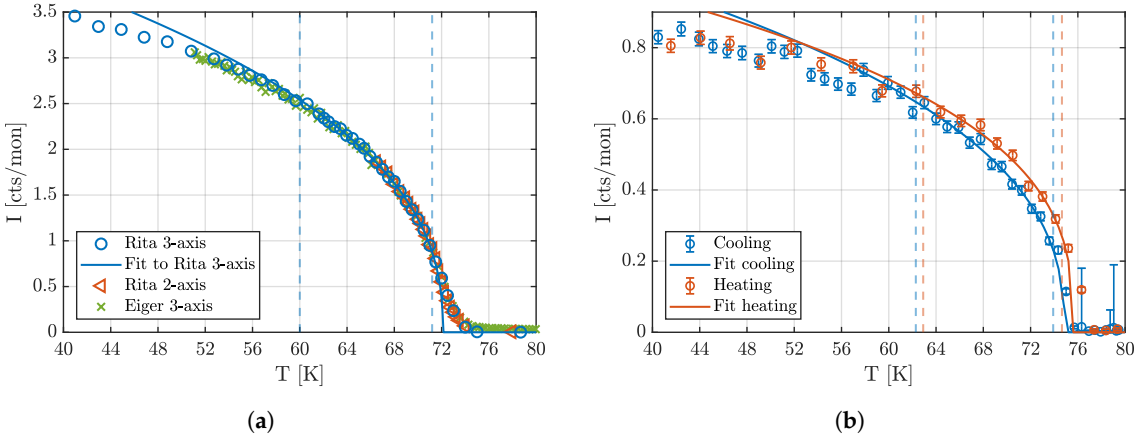

Figure 3. Fitted intensities of the magnetic Bragg peak at $\boldsymbol{q} = (100)$ as a function of temperature measured under different conditions. The fitting region is indicated by the coloured dashed lines. The resulting fit parameters can be seen in Table 1. (**a**) Data on YEMO under zero pressure. The data shown was measured using three different experimental setups: RITA-II three-axis mode, RITA-II two-axis mode, and Eiger three-axis mode. Error bars not shown, as they are smaller than the markers. (**b**) Data on YMO under a pressure of 1.5 GPa. We display both data taken during cooling and data taken during heating.

The measured intensities of the Bragg peak at $\boldsymbol{q} = (100)$ in YMO under a pressure of 1.5 GPa are shown in Figure 3b. Sample rotation scans in the (a, b) plane were performed while cooling and subsequently heating the pressure cell containing the sample. We see that the two curves shifted by

about 1.3 K due to the thermal drag of this procedure. In general, however, we note that the applied pressure increased T_N by 3–4 K. The true temperature dependence must be situated between these two curves.

Due to the lower counting statistics of the zero and high pressure experiments with YMO, it is harder to estimate the critical region based solely on the double logarithmic plots of the reduced temperature (shown in Figures A4 and A5 in the appendix). In order to be consistent, the same fitting range was used for the reduced temperature as for the YEMO data. After iteratively finding fitting ranges and finding T_N, the final fitting range for the high pressure YMO data was estimated as 62.3–73.9 K for the cooling data and 62.9–74.7 K for the heating data, which is indicated in Figure 3b as the red and blue dashed lines. For the cooling data, this yielded $T_N = 74.9(4)$ K and $\beta = 0.20(2)$, while the heating data yielded $T_N = 75.6(8)$ K and $\beta = 0.17(4)$. It should be noted that the two estimates for T_N are within 1.3 K of each other and that the two estimates for β are consistent within the statistical error, as expected. A naive average of the two values would estimate the true Néel temperature to be $T_N = 74.9(2)$ K and critical exponent to be $\beta = 0.19(2)$. For the YMO data under zero pressure, the very same fitting range was used as for the YEMO data, yielding $T_N = 71.3(5)$ K and $\beta = 0.22(2)$ upon heating (data not shown).

4. Experimental Results: Inelastic Neutron Scattering

In Figure 4, selected energy scans at a constant $\boldsymbol{q} = (100)$ measured at three temperatures are displayed for both YEMO under zero pressure and for YMO in applied pressure. The full dataset is shown in Figure A6 in the appendix. Two distinct magnon modes are observed at 1.6 K in zero pressure for YEMO in Figure 4a: one at 2.3 meV and one at 5.4 meV. These values are in complete agreement with literature for YMO [6,12,29]. The lower mode is gapped due to the anisotropy of the system. As the temperature is increased, the two modes move to lower energies. The lower mode increases in amplitude until 60 K, as expected from a Bose factor, and then falls off towards T_N. The width of the energy of the mode stays constant. At temperatures close to T_N, the quasi-elastic critical scattering broadens out from zero energy, making it increasingly difficult to follow the position of the lower mode. The upper mode has a constant integrated intensity from the base temperature until around 60 K, but here, the width of the mode increases. Above 60 K, the upper mode becomes very broad and its intensity decreases until it finally disappears at T_N. The constant $\boldsymbol{q}$ scans through the magnon modes reveal Gaussian-shaped peaks but with a pronounced skew. This skewness is due to a combination of the instrument resolution for the momentum transfer and the measurement at the minimum magnon mode where the density of states follows a step function. Close to T_N, a Lorentzian function with a centre in $\hbar\omega = 0$ meV was added to fit the critical quasi-elastic scattering. All fitting parameters can be found in Figure A8 in the appendix as functions of temperature.

Energy scans for YMO under an applied pressure of 1.5 GPa have been performed at four temperatures in an energy interval that covers the lower magnon mode (see Figure 4b). The magnon mode behaves qualitatively similar in pressure, moving to lower energies for higher temperatures. The signal to background ratio is 2 due to the small sample mass and the bulky sample environment. Despite this, a peak position can be found using a simple Gaussian function. A Lorentzian function was used to fit the broad elastic signal.

In Figure 5, the position of the lower spin wave mode is plotted as a function of temperature for both zero pressure (YEMO) and 1.5 GPa (YMO). For a skewed Gaussian, the centre and peak maximum are different and the difference depends on the skew parameter. We, therefore, chose to use the position of the peak maxima which was found numerically from the fitting function in Figure 5. It is naively assumed that the maximum positions have the same error as the peak centre found in the fitting routine. Despite the limited quality of the data in Figure 4b, the statistical uncertainty of the energy gap from the fitting routine remains consistently low at roughly 0.05 meV for the 1.5 GPa data and roughly 0.01 meV for the zero pressure data.

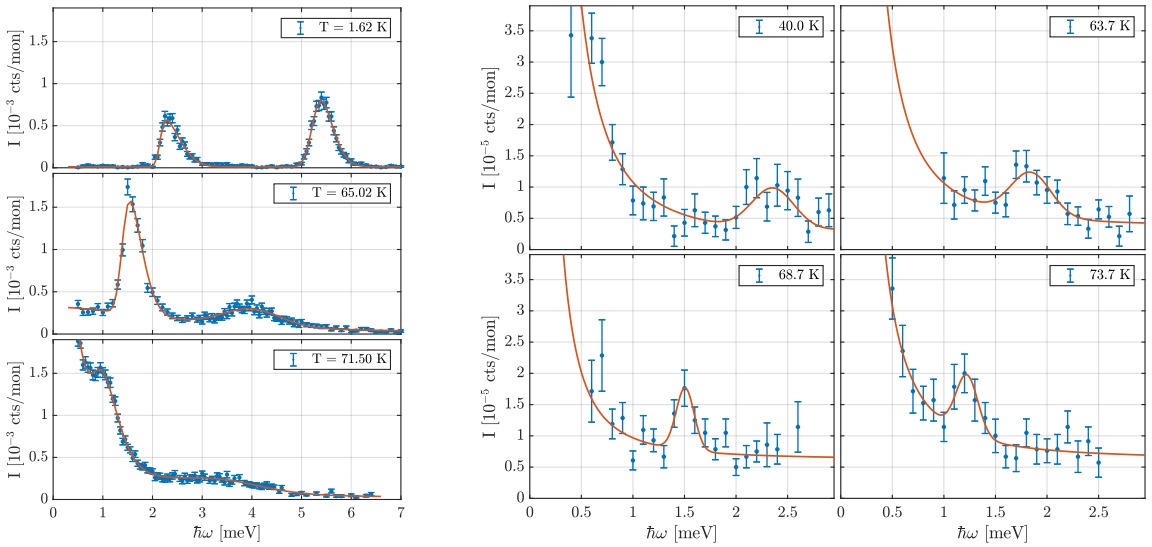

(**a**) (**b**)

Figure 4. Inelastic scans of energy transfer ($\hbar\omega$) above the magnetic Bragg peak at $\boldsymbol{q} = (100)$ showing the two magnon modes. (**a**) Measured intensities at selected temperatures for the zero pressure experiment on YEMO. (**b**) Intensities at all temperatures for the YMO experiment with an applied pressure of 1.5 GPa.

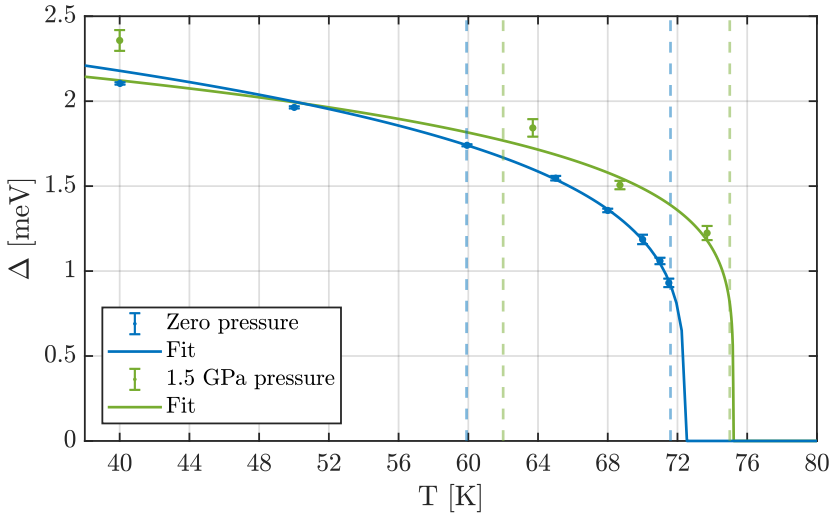

Figure 5. The anisotropy gap of the lower spin wave (Δ) as a function of temperature. The data was fitted with a power law in the critical ranges indicated by the dashed lines. Zero pressure data is from YEMO, while applied pressure data is from YMO.

The excitation gap, Δ, for spin waves in an anisotropic Heisenberg model, realized in YMO and YEMO, is expected to be proportional to the effective spin. This result from the spin-wave approach directly leads to the proportionality $\Delta \propto \langle S \rangle$ [30]. The excitation gap, also showing a critical behaviour ($\Delta \propto (1 - T/T_N)^{\beta'}$) is therefore expected to have the same critical exponent as the (sublattice) magnetization, $\beta = \beta'$. Indeed, the data in Figure 5 follows $\Delta \propto (1 - T/T_N)^{\beta'}$. For the zero pressure conditions, the data has been fitted in the same critical temperature range as the elastic data, namely 60–71.5 K. The critical parameters obtained were $T_N = 72.4(3)$ K and $\beta' = 0.24(2)$.

These parameters are consistent with the values obtained from the elastic data within one and two standard deviations respectively.

For the pressure data in Figure 5, it can be seen that the value of the gap is consistently higher under applied pressure compared with zero pressure. Since there are only three data points in the critical region for the inelastic data under applied pressure, an estimate of the critical exponent can be found by locking T_N to the naive average value obtained from the elastic measurements for heating and cooling ($T_{N(1.5GPa)} = 75.2(5)$ K). Fitting in the same critical range as for the data from the elastic measurements with applied pressure yields a critical exponent of $\beta' = 0.19(3)$, which is consistent with the value obtained from the elastic measurements within one standard deviation.

5. Discussion

We first note that, for clarity, the main results from this neutron scattering work are shown in Table 1, along with the corresponding literature results, where a number of experimental methods have been applied. We then proceed to discuss our findings individually.

Secondly, we note that some of our results were measured on pure *h*-$YMnO_3$ (YMO) and some with a low level of Eu doping (YEMO). In agreement with literature, the two samples differ so little in terms of physical and crystallographical properties that only elemental analysis (in our case gamma spectroscopy) can distinguish them. Therefore, we assume that their phase transition properties are strongly comparable, and below, we therefore discuss the two samples in combination.

Table 1. Summary table for the estimated critical temperatures, T_N, and critical exponents, β, for the various experiments in this work and in other publications. The data is for YMO, unless specifically stated otherwise. Our results for thermal-neutron triple axis spectrometer (TAS) and cold-neutron two-axis are not listed, but are consistent with the table values of our cold TAS data, as explained in the text.

	Zero Pressure		**1.5 GPa Applied Pressure**	
	T_N **[K]**	β **(**β'**)**	T_N **[K]**	β **(**β'**)**
Current work Neutron diffraction, cold TAS	71.3(1) (YMO) 72.11(5) (YEMO)	0.22(2) (YMO) 0.206(3) (YEMO)	Cooling: 74.9(4) Heating: 75.6(8)	Cooling: 0.20(2) Heating: 0.17(4)
Current work Neutron inelastic, cold TAS	72.4(3) (YEMO)	0.24(2) (YEMO)	Locked to 75.2	0.19(3)
Roessli et al. [10] Neutron diffraction, cold TAS	72.10(5)	0.187(2)	–	–
Chatterji et al. [12] Neutron diffraction, thermal TAS	69.98(5)	0.295(8)	–	–
Kozlenko et al. [14] Neutron powder diffraction	75	–	Extrapolated: 76.8	–
Lancaster et al. [13] μSR	74.7(3)	0.35(3)	Extrapolated: 78.35	–
Poirier et al. [11] Ultrasound	72.43(5)	0.42(3)	–	–

5.1. The Critical Parameters and the Critical Region

The magnetic phase transition in YMO at zero pressure has been strongly debated in the literature, as we discuss below.

The traditional approach to finding T_N and β in neutron diffraction is to fit the scattering signal with two components: a resolution limited Gaussian and a broader Lorentzian signal from the critical scattering close to T_N. This approach was not applicable in our experiment, since the width of the signal stayed constant as seen in Figure A1. Instead, we used the double-logarithmic method described in Section 3. We believe this to be a robust approach to determine the critical diffraction signal. With this method, an unwanted signal from critical scattering peaking at T_N would reveal itself as an upturn of the signal at low values of t in the double-logarithmic plot. On the other hand, the effects of extinction and deviation from universality at lower temperatures would be revealed as a downturn

from the linear behaviour in the double-logarithmic plot at high values of the reduced temperature t, and therefore be discarded by the method, as demonstrated in the Appendix. A linear behaviour over a large t-range in the double-log plot would indicate that none of these effects are present and that the critical behaviour analysis is therefore valid.

We measured the phase transition with three different neutron scattering methods with energy resolutions of, respectively, 0.2 meV, 1 meV, and about 5 meV. These three methods yield very different integration of quasielastic fluctuations just around T_N. However, all were found to display the same critical behaviour, as seen in Figure 3a, again indicating the robustness of our method for this particular system.

Roessli et al. used a cold-neutron triple axis instrument with an energy resolution of $\Delta E = 0.18$ meV (FWHM) and found $T_N = 72.10(5)$ K and $\beta = 0.187(2)$ [10]. Their range of fitting the critical behaviour is not directly mentioned in their publication, but from their illustrations, it seems to be 66 K to 71 K. As in the analysis of our present work, they discard the weak signal above T_N as critical scattering.

In contrast, Chatterji et al. found the Néel temperature from thermal neutron two-axis diffraction to $T_N = 69.98(5)$ K with a critical exponent of $\beta = 0.295(8)$, using a critical range for the fit of 60 K through 69.5 K [12], a range very similar to the one used by us. They attribute the difference to Roessli et al. [10] to that group's use of a non-critical T-range for the fitting (although we deem the fitting ranges of the two groups to be fairly similar). Curiously, no indication of critical scattering above T_N is present in their data (as compared to our Figure 3a). This could be an indication of difference in data analysis from our work—or a problem with quality of their sample. In any case, since the underlying data of Chatterji et al. is so qualitatively different from ours, it is unsurprising that our values of T_N and β differ.

The critical parameters were also estimated from muon spin rotation (μSR) by Lancaster et al. [13]. They found $T_N = 74.7(3)$ K with a critical exponent of $\beta = 0.35(3)$. For the determination of T_N, Lancaster et al. used the midpoint between 0% and 100% ordered volume fraction, which is a 4 K wide temperature range [13]. The muon is a local probe that measures on a very long time scale (~µs) compared to that of neutron scattering (~ps). Hence, the ordering temperature measured by μSR is likely to be slightly lower than that measured by neutron scattering. The difference in time scale can therefore not explain the difference in the critical temperatures measured with the two methods. One explanation for the higher T_N could be impurities in their sample which would be able to lift the frustration locally, thereby also giving a distribution of ordering temperatures. For the determination of β, Lancaster et al. fitted a stretched exponential to the full temperature range from 2 K and up [13]. In our view, this weakens the validity of their data analysis. The three data points within the critical region close to the critical temperature lay on a curve that is also consistent with a β of around 0.2 if a value of T_N just above 72 K is assumed.

Poirier et al. [11] used ultrasound measurements to estimate the critical parameters. They obtained $T_N = 72.43(5)$ K and $\beta = 0.42(3)$. Their estimate of the Néel temperature is consistent with our results, while the critical exponent differs significantly. The ultrasound method is an indirect spin probe, and it is sensitive to elastic deformations of the crystal structure. A strong magneto-elastic coupling was reported by Lee et al. [8] after Poirier et al. presented their work [11]. Lee et al. claimed to observe a relative shift in the Mn position of 3.3% over the critical region in temperature. This was not taken into account in the data analysis by Poirier et al. which could explain the discrepancy between their results and ours.

Although we used a non-standard method instead of the usual two-component method for analysing critical scattering, we still observed identical trends and values for the critical behaviour over a range of different experiments and two different samples. For this reason, and due to the similarity between our data and those of Roessli et al. [10], we deem it likely that our present results give an accurate account of the critical temperature, $T_N = 72.11(5)$ K for YEMO, and the critical exponent $\beta \approx 0.21$ for both samples.

Turning to the precise value of the Néel temperature, Eu doping was earlier found to slightly lower T_N [17], so in the light of our results for YEMO, it is likely that the true value for YMO lies in

the range 72–74 K. In addition, the μSR data, although potentially less accurate, definitely shows an ordered moment at 72 K. For that reason, it must be concluded that the Néel temperature of h-$YMnO_3$ is at least of that value, questioning the findings of Chatterji et al. [12]. In addition, the critical exponents agree fairly well between our work and that of Roessli et al. ($\beta = 0.187(2)$) [10], adding to the confidence in our results.

Discussing the inelastic measurements, Chatterji et al. investigated the T-dependence on the spin wave spectrum [12]. However, that group did not report the spin wave spectrum close to the Néel temperature. In addition, they measured the spin wave spectrum only at points in the reciprocal space away from the Γ-point in reciprocal space. Although not explicitly mentioned, the energy resolution of their scans indicated that the temperature dependence was taken using a thermal-neutron triple axis instrument, so they were only to follow the lowest lying excitation only down to 1.8 meV, which happens more than 10 K from T_N. In our work, we measured the spin excitations at the Γ-point, where the excitations have no dispersion. In addition, we used a cold-neutron triple axis with a superior energy resolution, allowing us to follow the lowest energy excitation down to 0.6 meV (1.2 meV in pressure), which took place less than 1 K (1.5 K in pressure) away from T_N. For this reason, we were able to follow the closure of the spin wave gap closer to the phase transition, making our measurements a more reliable account of the critical behaviour of the inelastic scattering.

5.2. Pressure Effect of the Magnetic Order and Phase Transition

Based on our elastic data and using the same approach as described above, we found that an applied pressure of 1.5 GPa increased the ordering temperature with 3.9 K from $T_{N(0\,GPa)} = 71.3(5)$ K to $T_{N(1.5GPa)} = 75.2(5)$ K. This is in general agreement with earlier neutron diffraction studies by Kozlenko et al. [14,19]. They showed that the pressure indeed increases the Néel temperature, and based on measurements at zero pressure and applied pressures of 6.7 GPa, they estimated a linear relationship of the form $T_N = 75.0 + 1.2p$ K, where p is the pressure in GPa, which extrapolates to $T_N = 76.8$ K at $p = 1.5$ GPa. They attributed this to the increase in exchange interaction when the volume—and thus the inter-atomic distances—decreases. This slope is significantly smaller than the results of our single crystal neutron studies and the muon studies. This indicates that the change of the Néel temperature is not linear at higher pressures.

The refinement of the magnetic data in Ref. [19] shows that the spin direction of the Mn^{3+} ions turn gradually 90° between 0 and 9 GPa, going from the pure Γ_1 structure over a mixed $\Gamma_1 + \Gamma_2$ structure to a pure Γ_2 structure at 9 GPa. The ordered moment decreases from 3.27 μ_B at zero pressure to 1.52 μ_B at 5 GPa. Kozlenko et al. [14] and earlier, Park et al. [31] attributed this to the concurrent existence of a spin liquid phase. This phase is also claimed to be responsible for the lowering of the ordered magnetic moment at zero pressure from the expected 4.0 μ_B for ($S = 2$) Mn^{3+}, as well as for the increase in diffuse scattering at the Néel temperature and at the applied pressure. This effect was attributed to the restoration of perfect triangular symmetry within the layers by pressure. We note, at this point, that the observed anisotropy gap under pressure slightly increased (see Figure 5). This challenges the interpretation in terms of a Heisenberg model at first sight, because the anisotropy gap should be proportional to the ordered moment which was found to be reduced. At the same time, the Néel temperature increased, indicating that the couplings responsible for the proportionality constant were increasing as well, that is, there is no contradiction if the product of these two values slightly increases.

μSR at zero pressure shows that the magnetic phase has only one long-range ordered component, and no spin-liquid component was identified [13]. Under pressure, the muon data show that there was no change in magnetic volume fraction, which was attributed to a pressure-induced spin-liquid phase. The Néel temperature scaled with a pressure of up to 1.4 GPa as $T_N = 74.0 + 2.9p$ K [13]. The authors suggested two reasons for this behaviour: (a) the frustration is more perfect under applied pressure, and (b) the out-of-plane couplings are assumed to increase with pressure.

Our in-pressure neutron diffraction study shows a good agreement with this behaviour with a slope of around 2.6 K/GPa; with the present uncertainties, the deviation from the earlier study was not significant. Additionally, we measured the critical exponent of YMO to $\beta = 0.19(2)$ which agrees with the zero pressure data of $\beta = 0.22(2)$ within error bars.

The spin excitations at the Γ point were also measured under applied pressure, allowing us to track the anisotropy gap as a function of temperature. At $T = 40$ K, the anisotropy gap in pressure was increased by 0.25 meV at $p = 1.5$ GPa compared with the zero pressure data. Though the Néel temperature could not be determined independently for the inelastic data, the critical exponent was obtained to be $\beta = 0.19(3)$, in accordance with our neutron diffraction measurements. It should be noted that this analysis was based on only three data points; however, the results are consistent with the elastic data in applied pressure shown in Figure 3b, and should thus be taken only as corroboration of this result.

5.3. The Universality Class of h-YMnO$_3$

The magnetic excitations in *h*-$YMnO_3$ can be well understood in terms of a Heisenberg model with an in-plane anisotropy. The exchange interactions are strongly frustrated and couple the spins in all three directions, whereas the coupling out of plane were earlier found by us to be at least one order of magnitude smaller [23]. The anisotropy in spin space makes the one-to-one assignment of this system to a universality class difficult. In our experiments, we deduce the critical exponent β to be in the range of β = 0.17–0.24, with a clear majority of data in the range 0.19–0.22. All these values are consistent within their standard deviations.

Looking up critical exponents from the literature, we found values of $\beta = 0.19$ for the 3D Ising model, $\beta = 0.25$ for 2D Chiral XY system, $\beta = 0.30$ for a chiral Heisenberg model, and an even larger exponent for the 3D Heisenberg model [15]. Note that a smaller critical exponent leads to a larger order parameter close to the critical region. In the Ising model, only fluctuations of one type are present, thus allowing for a larger order parameter and thus, a smaller critical exponent. Moving towards the XY model or the Heisenberg model, two or three components of the spin operator are allowed to fluctuate, thus suppressing the order parameter more strongly and increasing the critical exponent.

Firstly, we note that despite the 3D Ising model having a close match with the critical exponent in our data, such a model is not capable of explaining the inelastic neutron data from our earlier experiments [23]. Secondly, even though the 2D or 3D Heisenberg models with fluctuations in all spin components seem to be the most relevant models, the critical exponent of these models does not match our observations at all. In contrast, the fluctuations in the frustrated, anisotropic system were found to be much less effective, as testified by the measured small critical exponent of our investigation. We should note here that for the material VCl_2, which is also an anisotropic triangular antiferromagnet, a value of $\beta = 0.20$ has been measured—remarkably close to our findings [15,32]. We find it likely that the strong frustration in both materials is causing this behaviour at criticality, strengthening the case for a separate universality class for frustrated antiferromagnets. At this point, we would like to mention a subtle difference between the phase transition of an ordinary Heisenberg magnet and a stacked antiferromagnet which is also among the proposed magnetic ground states [22]. The latter additionally possesses a Z_2 order parameter of vector-spin-chirality [33] which could already be broken above T_N. In this case, the corresponding phase transition would be equivalent to that of an ordinary Heisenberg magnet. At this point, we do not consider this possibility further, because the magnetic chirality is expected not to couple to the ferroelectic order parameter that breaks a similar symmetry at much higher temperatures. The reasons for this are (i) the different mechanisms of both phase transitions manifesting themselves in ordering temperatures that differ by more than one order of magnitude, and (ii) the expectation that a spin-lattice coupling only sets in once the long range magnetic order is also present.

The application of hydrostatic pressure changes the distances between the magnetic ions in *h*-$YMnO_3$; thus, the values of the exchange interactions are expected to change as well. Considering

that the effect of pressure is stronger in the plane, because the relative change of the lattice constant a is larger than the relative change of the constant c [34], a stronger effect on the in-plane couplings is also expected. This is also in accordance with the observation that the magnon–phonon coupling as observed in earlier experiments [23] can be solely modelled by a modulation of the in-plane couplings, the same modulation that takes place by the static change of the distance between the magnetic ions upon application of pressure. An increased critical temperature as observed in our work, could be explained by an increase in these couplings, keeping in mind that the out-of plane couplings are necessary for order in a Heisenberg model. Turning now to the consequences of the pressure on the universality class of the system, we found no experimental evidence for a change in the value of β upon the application of pressure. Thus, there is no indication that the universality class is altered by pressure.

6. Conclusions

We carefully studied the antiferromagnetic magnetic phase transitions of h-$YMnO_3$ and h-$(Y_{0.98}Eu_{0.02})MnO_3$ by neutron diffraction. For the Eu-doped sample, the Néel temperature was found to be consistent between the three different set-ups: $T_N = 72.11(5)$ K. For the pure sample, we found $T_N(0\,\text{GPa}) = 71.3(5)$ K, whereas this temperature increased under applied pressure to $T_N(1.5\,\text{GPa}) = 75.2(5)$ K.

The critical exponents agree within error bars for the two samples and under zero and applied pressure, namely $\beta = 0.206(3)$ for the doped sample and $\beta(0\,\text{GPa}) = 0.22(2)$ and $\beta(1.5\,\text{GPa}) = 0.19(2)$ for the pure sample. In our view, this favours the previous results of Roessli et al. over the rather different findings of Chatterji et al. [12].

From inelastic neutron scattering, we found that the anisotropy gap in the spin wave spectrum closes in almost the same way as for the diffraction measurements. Assuming that $\Delta \propto \langle S \rangle$, we found ordering temperatures of 72.4(3) K and 75.2(5) K for zero and applied pressure, respectively. The critical exponents were also very similar with values of $\beta = 0.24(2)$ and $0.19(3)$, respectively. Thus, applying pressure to the system does not change the critical exponent within our statistical errors.

The low value of $\beta \approx 0.20$ found consistently in all our measurements is in agreement with that of the similar material VCl_2. A possible explanation for this is that frustrated triangular magnets are in a separate universality class with an unusually low value of β.

Author Contributions: S.H.-D. and K.L. conceived and designed the experiments; S.H.-D., J.S.W., A.L.F., and K.L. performed the experiments; E.P. produced the single crystal YMO sample; S.J. and S.H.-D. analyzed the data; A.K. contributed to the data interpretation and discussion; S.H.-D., S.J., A.K. and K.L. wrote the manuscript with input from all co-authors.

Funding: The project was funded by the Danish Research Council "Det Frie Forskningsråd, Nature og Univers" through "DANSCATT".

Acknowledgments: This work is based on experiments performed at SINQ, Paul Scherrer Institute (Villingen, Switzerland). We would like to thank Henrik M. Rønnow for useful comments on our data analysis, Ch. Niedermayer for assistance with neutron scattering measurements, and Dharmalingam Prabhakaran for correspondence regarding the sample.

Conflicts of Interest: The authors declare no conflict of interest.

Appendix A. Diffraction Data Fits

The datasets for the elastic zero pressure on YEMO were fit with a single Gaussian for each temperature, and the fitting parameters are shown in Figure A1. The amplitude was used to find the Néel temperature and critical exponent, but before performing the fit, the critical range was determined. This was done by plotting the amplitude versus the reduced temperature, $t = (T - T_N)/T_N$, on a double logarithmic plot for a range of possible Néel temperatures, as shown in Figure A2. A straight line was overlain and fitted to the middle data points. Finding the region where the points were linear in the longest range of reduced temperatures yields a fair estimate of T_N, as well as the extent

of the critical region. A detailed estimate of T_N can then be obtained by fitting a power law to the amplitude versus temperature, and iteratively checking the length of the critical region. For the elastic, zero pressure data, the critical region was estimated as $T = 60$–71.2 K, corresponding to a reduced temperature region of $t = 0.013$–0.17 for the final estimate of $T_N = 72.11(5)$ K, as obtained via the power law in Figure 3a.

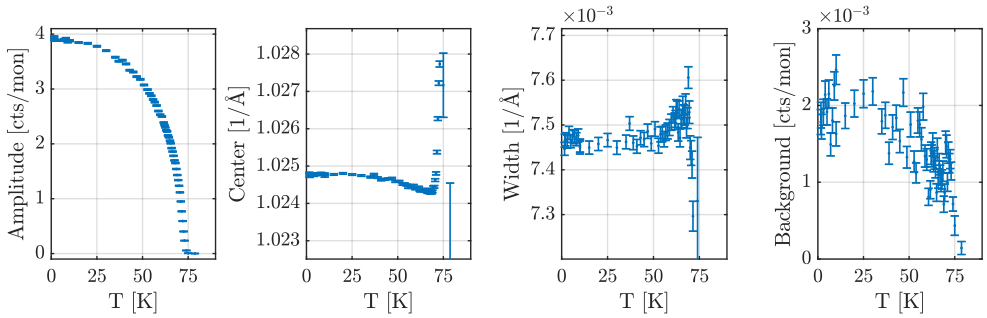

Figure A1. Overview of the parameters used in the Gaussian fits for the elastic zero pressure data for YEMO at the $\boldsymbol{q} = (100)$ magnetic Bragg peak measured at RITA-II in triple-axis mode. Figures show from left to right: amplitude, centre, width, and background.

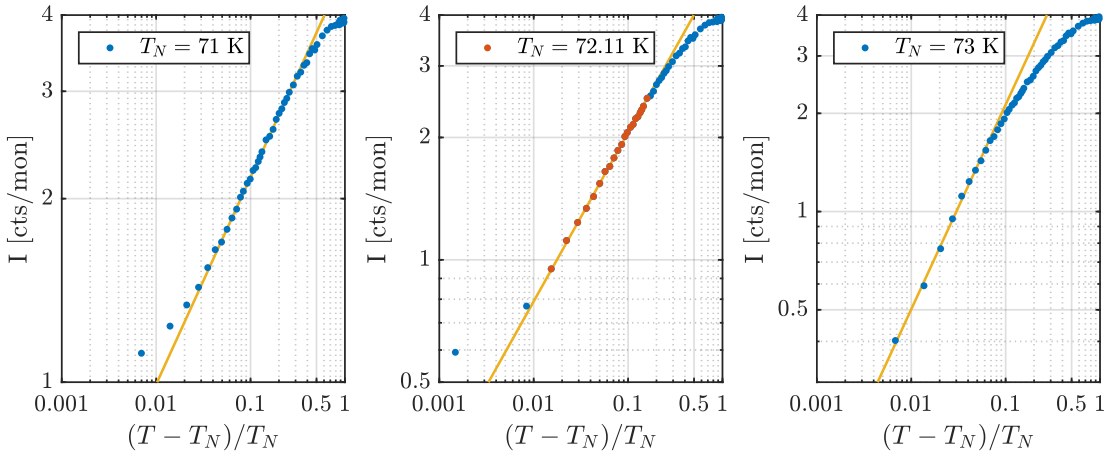

Figure A2. Zero pressure double-logarithmic plot for various estimates of T_N (YEMO), as well as the true $T_N = 72.11(5)$ K obtained from the fit in Figure 3a. The straight lines are overlain as a guide to the eye. For the value of $T_N = 72.11$ K, the linear range for fitting is estimated as 60–71.2 K.

For the elastic applied pressure data on YMO, a similar approach was used for the cooling and heating data independently of each other. For each dataset, the Gaussian fitting parameters are shown in Figure A3. However, due to the poorer quality of data, it was harder to use the double logarithmic plots in Figures A4 and A5 to estimate the true critical region. Thus, for consistency, the critical region was estimated based on the reduced temperature range from the elastic zero pressure data, namely $t = 0.013$–0.17, based on their respective Néel temperatures. Performing the same iterative process as described above, this yields a critical range of 62.3–73.9 K for the cooling data and 62.9–74.7 K for the heating data. The fit shown in Figure 3b yielded values for the Néel temperature and critical exponent of $T_N = 74.9(4)$ K and $\beta = 0.20(2)$ for the cooling data, and $T_N = 75.6(8)$ K and $\beta = 0.17(4)$ for the heating data. It should be noted that the estimates for T_N were 0.7 K apart and consistent with each other within the statistical errors. The estimates of β were also consistent within the errors.

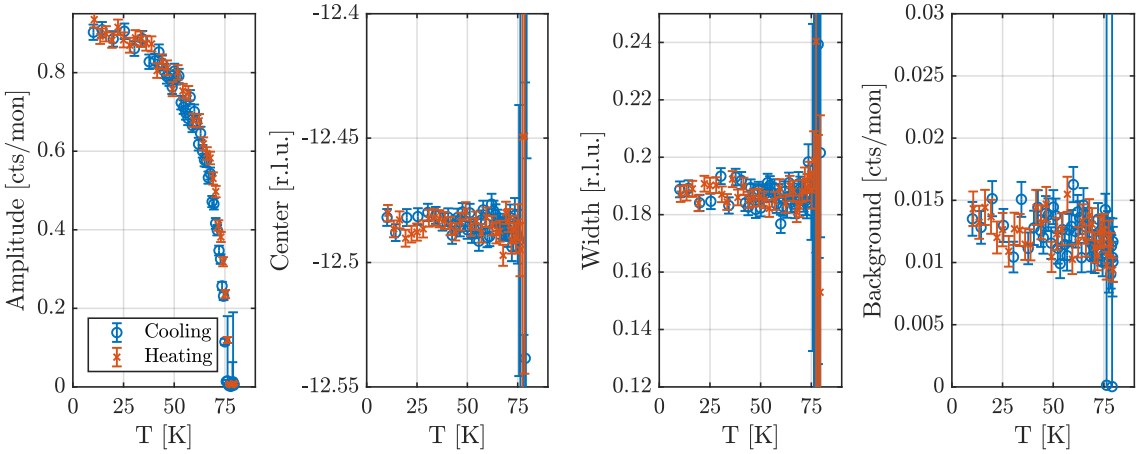

Figure A3. Overview of the parameters used in the Gaussian fits for the elastic applied pressure (1.5 GPa) data for YMO at the $\boldsymbol{q} = (100)$ magnetic Bragg peak measured at RITA-II in triple-axis mode. Figures show from left to right: amplitude, centre, width, and background.

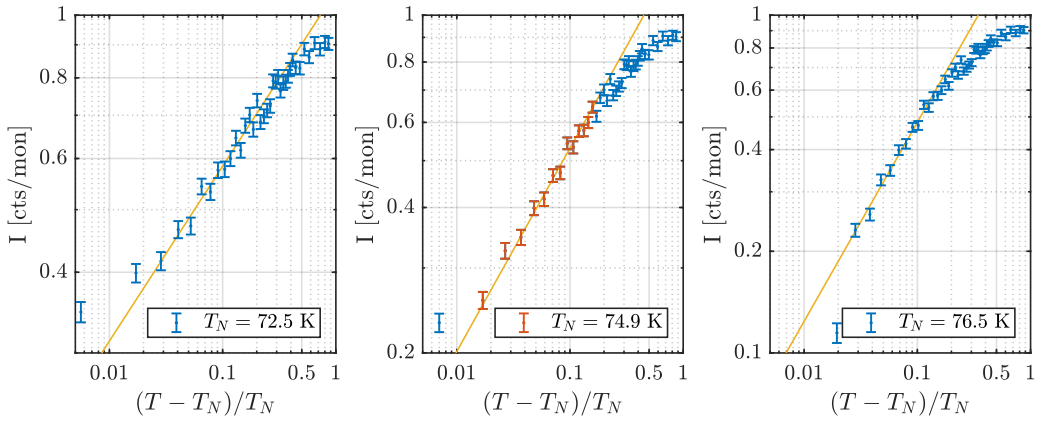

Figure A4. Double logarithmic plot for the applied pressure data taken while cooling the YMO sample for various estimates of T_N, as well as the true T_N obtained from the fit in Figure 3b, $T_\mathrm{N} = 74.9(4)$ K. The straight lines are overlain as a guide to the eye. For the value of $T_\mathrm{N} = 74.9$ K, the linear range for fitting was estimated to be 62.3–73.9 K.

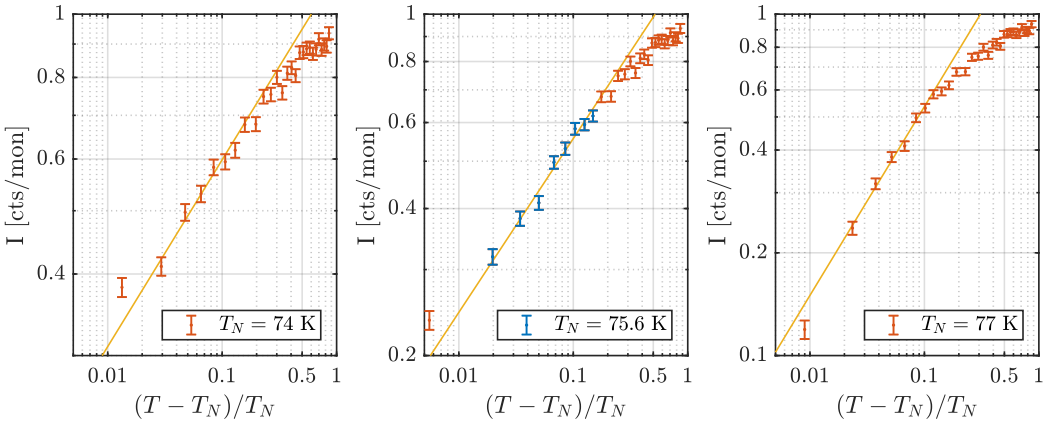

Figure A5. Double logarithmic plot for the applied pressure data taken while heating the YMO sample for various estimates of T_N, as well as the true T_N obtained from the fit in Figure 3b, $T_\mathrm{N} = 75.6(4)$ K. The straight lines are overlain as a guide to the eye. For the value of $T_\mathrm{N} = 75.6$ K, the linear range for fitting was estimated to be 62.9–74.7 K.

Appendix B. Inelastic Neutron Scattering Data

The inelastic data for YEMO under zero applied pressure is shown in Figure A6, while the inelastic data for YMO under applied pressure is shown in Figure 4b. For temperatures below $T = 71.75$ K, the peaks were deemed to be sufficiently separated to allow fitting to extract the peak position. The data was fitted with the function below, consisting of two skewed Gaussians for the magnon modes and a Lorentzian centred at $E = \hbar\omega = 0$ near T_N for the elastic signal.

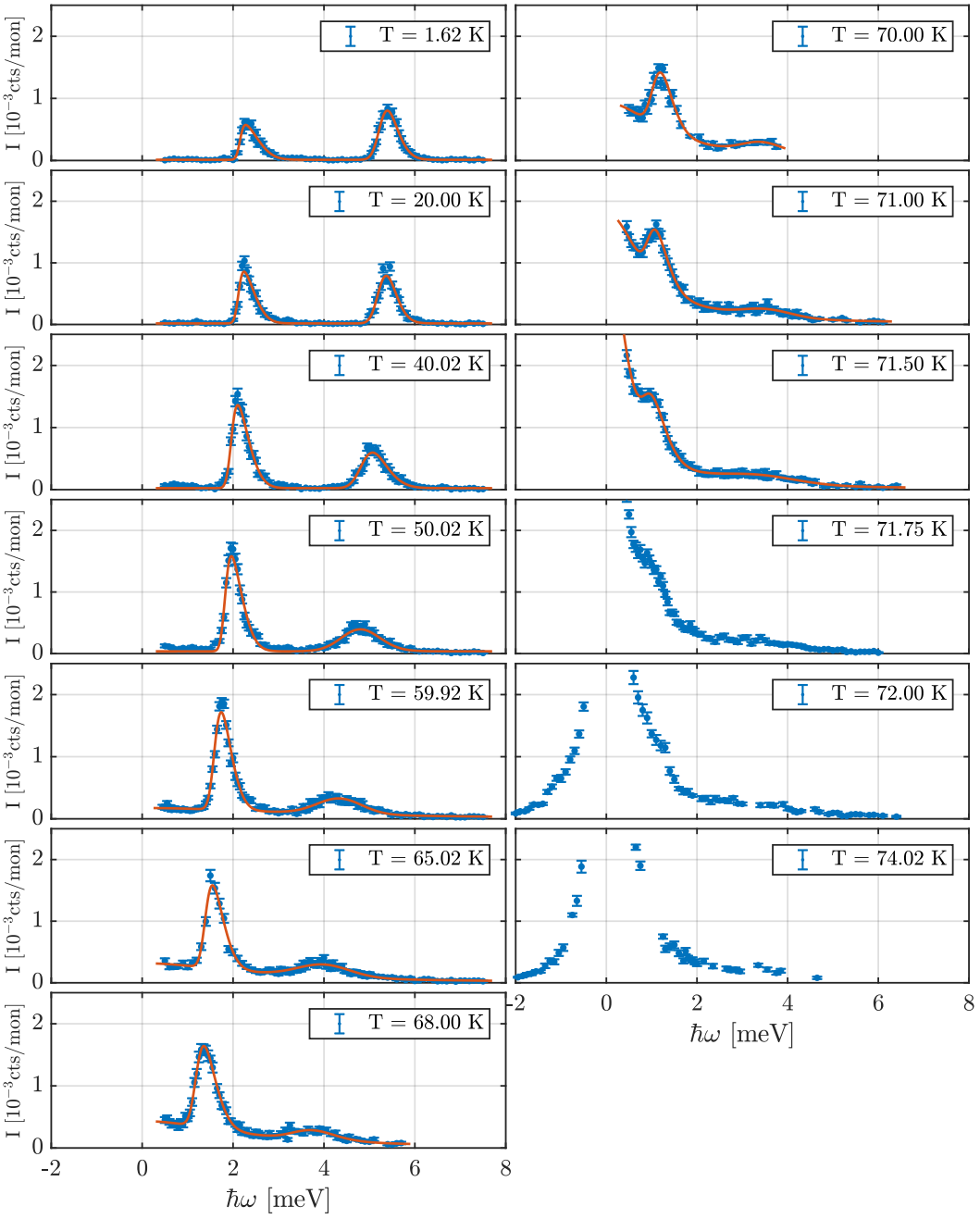

Figure A6. Inelastic energy scans of YEMO at zero pressure showing the peak shape.

$$
\begin{aligned}
I(E) &= I_{\text{magnon}_1}(E) + I_{\text{magnon}_2}(E) + I_{\text{Lorentz}}(E) \\
&= \frac{I_1}{\sqrt{2\pi}\sigma_1} \exp\left(-\frac{(E-\mu_1)^2}{2\sigma_1^2}\right) \left[1 + \text{erf}\left(\frac{\gamma_1(E-\mu_1)}{\sqrt{2}\sigma_1}\right)\right] \\
&\quad + \frac{I_2}{\sqrt{2\pi}\sigma_2} \exp\left(-\frac{(E-\mu_2)^2}{2\sigma_2^2}\right) \left[1 + \text{erf}\left(\frac{\gamma_2(E-\mu_2)}{\sqrt{2}\sigma_2}\right)\right] \\
&\quad + I_0 \frac{\sigma_0^2}{E^2 + (\sigma_0/2)^2} + Bkg,
\end{aligned}
$$

where I_j refers to the peak intensity, σ_j to the width, μ_j to the peak centre, γ_j to the peak skewness, and Bkg to the background. Additionally, the subscript 1 refers to parameters for the lower magnon mode; subscript 2 refers to the upper magnon mode; and subscript 0 refers to the elastic mode. The fitting parameters for this function versus temperature for the zero pressure data can be seen in Figure A8. Also shown is the integrated intensity for each magnon: $\int Idq = \sum I_j \sigma_j$.

The inelastic data for YMO under applied pressure is shown in Figure 4b. The data was fitted with a Gaussian and a Lorentzian in $\hbar\omega = 0$, as described in the formula above. However, since the data is of poorer quality, allowing for a variable skew cannot be justified, and the skew for the magnon was locked to $\gamma = 0$. Additionally, the width of the Lorentzian was fixed to the appropriate width for the $T = 40$ K data.

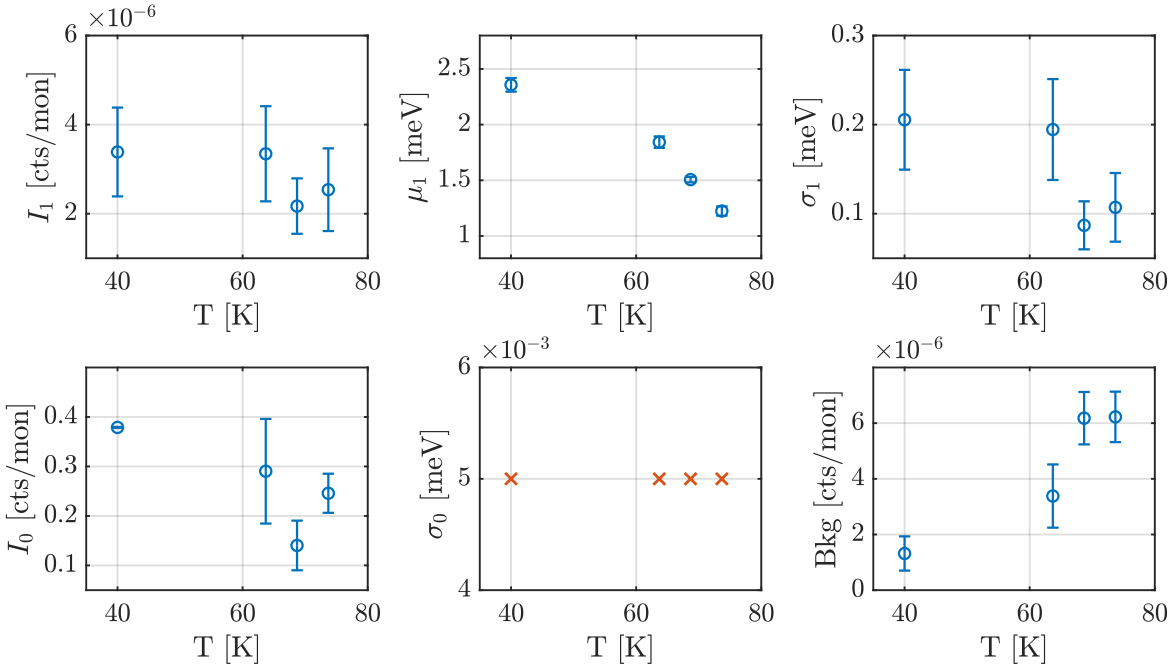

Figure A7. Fitting parameters of the inelastic YMO measurements under applied pressure (1.5 GPa). The upper row are parameters pertaining to the lower magnon mode, and the lower row pertains to the elastic peak, as indicated by the respective subscripts. I is the peak intensity, σ the width, and μ the peak centre, and Bkg refers to the background. The locked fitting parameters are marked as red crosses.

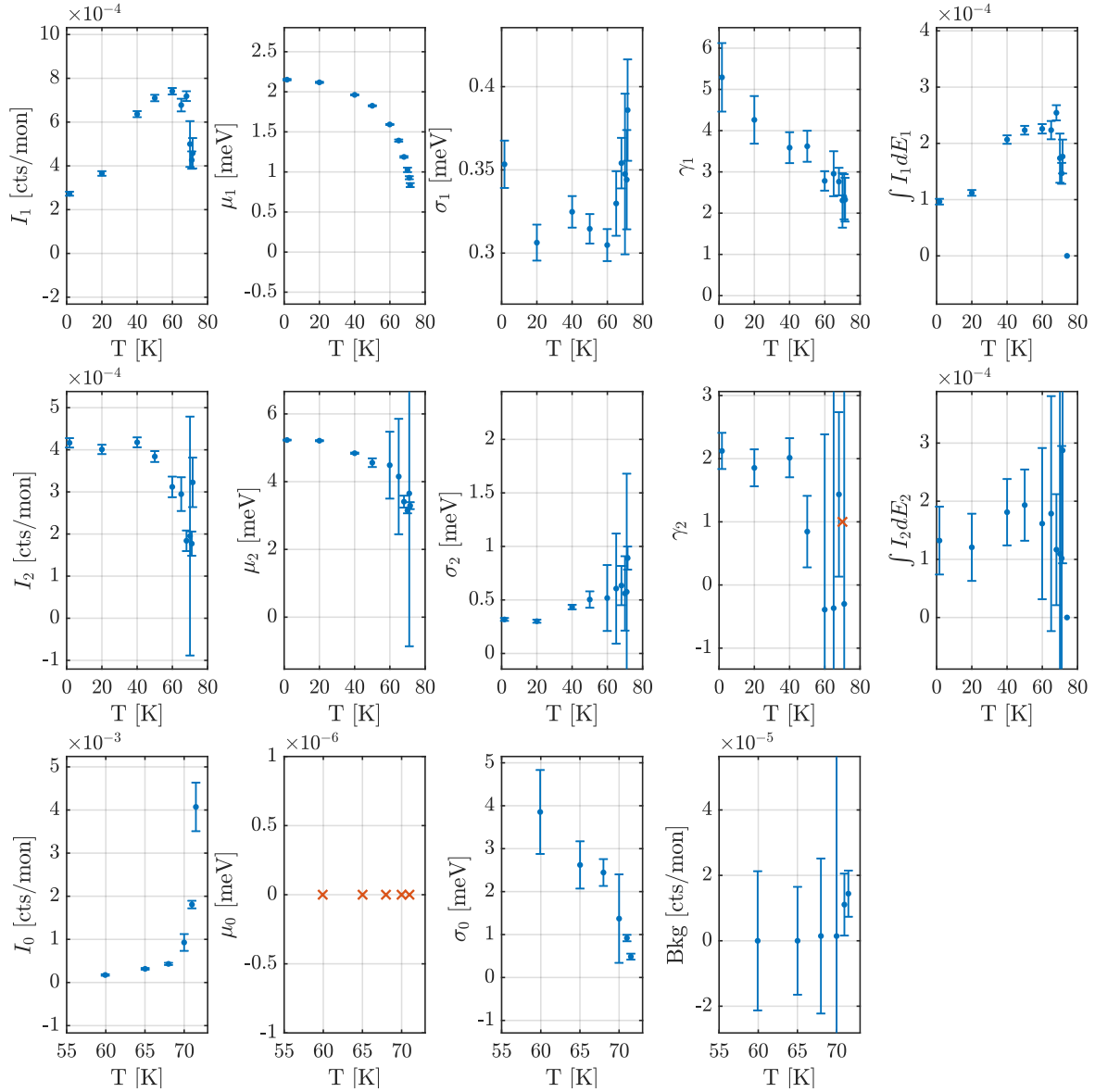

Figure A8. Fitting parameters and integrated intensity of the inelastic YMO measurements under zero pressure. Here, the upper row represents parameters pertaining to the lower magnon mode; the middle row pertains to the upper magnon mode; and the lower row pertains to the elastic peak, as indicated by the respective subscripts. I is the peak intensity, σ_j is the width, μ_j is the peak centre, γ_j is the peak skewness, *Bkg* refers to the background, and $\int Idq$ to the integrated intensity. The locked fitting parameters are marked as red crosses.

References

1. Hill, N.A. Why Are There so Few Magnetic Ferroelectrics? *J. Phys. Chem. B* **2000**, *104*, 6694–6709. [CrossRef]
2. Lee, S.; Ratcliff, W.; Cheong, S.W.; Kiryukhin, V. Electric field control of the magnetic state in $BiFeO_3$ single crystals. *Appl. Phys. Lett.* **2008**, *92*, 192906. [CrossRef]
3. Catalan, G.; Scott, J.F. Physics and Applications of Bismuth Ferrite. *Adv. Mater.* **2009**, *21*, 2463. [CrossRef]
4. Spalding, N.A.; Fiebig, M. The renaissance of Magnetoelectric Multiferroics. *Science* **2005**, *309*, 391–392. [CrossRef] [PubMed]
5. Cheong, S.W.; Mostovoy, M. Multiferroics: A magnetic twist for ferroelectricity. *Nat. Mater.* **2007**, *6*, 13–20. [CrossRef] [PubMed]

6. Petit, S.; Moussa, F.; Hennion, M.; Pailhès, S.; Pinsard-Gaudart, L.; Ivanov, A. Spin Phonon Coupling in Hexagonal Multiferroic $YMnO_3$. *Phys. Rev. Lett.* **2007**, *99*, 266604. [CrossRef] [PubMed]
7. Sim, H.; Oh, J.; Jeong, J.; Le, M.D.; Park, J.G. Hexagonal $RMnO_3$: A model system for two-dimensional triangular lattice antiferromagnets. *Acta Cryst. B* **2016**, *72*, 3–19. [CrossRef] [PubMed]
8. Lee, S.; Pirogov, A.; Kang, M.; Jang, K.H.; Yonemura, M.; Kamiyama, T.; Cheong, S.W.; Gozzo, F.; Shin, N.; Kimura, H.; Noda, Y.; Park, J.G. Giant magneto-elastic coupling in multiferroic hexagonal manganites. *Nature* **2008**, *451*, 805–808. [CrossRef] [PubMed]
9. Gibbs, A.S.; Knight, K.S.; Lightfoot, P. High-temperature phase transitions of hexagonal $YMnO_3$. *Phys. Rev. B* **2011**, *83*, 094111. [CrossRef]
10. Roessli, B.; Gvasaliya, S.N.; Pomjakushina, E.; Conder, K. Spin fluctuations in the stacked-triangular antiferromagnet $YMnO_3$. *J. Exp. Theor. Phys. Lett.* **2005**, *81*, 287–291. [CrossRef]
11. Poirier, M.; Laliberté, F.; Pinsard-Gaudart, L.; Revcolevschi, A. Magnetoelastic coupling in hexagonal multiferroic $YMnO_3$ using ultrasound measurements. *Phys. Rev. B* **2007**, *76*, 174426. [CrossRef]
12. Demmel, F.; Chatterji, T. Persistent spin waves above the Néel temperature in $YMnO_3$. *Phys. Rev. B* **2007**, *76*, 212402. [CrossRef]
13. Lancaster, T.; Blundell, S.J.; Andreica, D.; Janoschek, M.; Roessli, B.; Gvasaliya, S.N.; Conder, K.; Pomjakushina, E.; Brooks, M.L.; Baker, P.J.; et al. Magnetism in Geometrically Frustrated $YMnO_3$ under Hydrostatic Pressure Studied with Muon Spin Relaxation. *Phys. Rev. Lett.* **2007**, *98*, 197203. [CrossRef] [PubMed]
14. Kozlenko, D.P.; Mirebaeu, I.; Park, J.G.; Goncharenko, I.N.; Lee, S.; Park, J.; Savenko, B.N. High-pressure-induced spin liquid phase of multiferroic $YMnO_3$. *Phys. Rev. B* **2008**, *78*, 054401. [CrossRef]
15. Collins, M.F.; Petrenko, O.A. Triangular antiferromagnets. *Can. J. Phys.* **1997**, *75*, 605–655. [CrossRef]
16. Murtazaev, A.K.; Ramazanov, M.K.; Badiev, V.K. Phase Transitions and Critical Properties of the Frustrated Heisenberg Model on a Layer Triangular Lattice with Next-to-Nearest-Neighbor Interactions. *J. Exp. Theor. Phys.* **2012**, *115*, 303–308. [CrossRef]
17. Namdeo, S. Synthesis and Characterization of Novel Perovskite Multiferroics. Ph.D. Thesis, Devi Ahilya University, Indore, India, 2014.
18. Goian, V.; Kamba, S.; Kadlec, C.; Nuzhnyy, D.; Kuzel, P.; Moreira, J.A.; Almeida, A.; Tavares, P. THz and infrared studies of multiferroic hexagonal $Y_{1-x}Eu_xMnO_3$ ($x = 0 - 0.2$) ceramics. *Phase Transit.* **2010**, *83*, 931–941. [CrossRef]
19. Kozlenko, D.P.; Kichanov, S.E.; Lee, S.; Park, J.G.; Savenko, B.N. Pressure-induced spin fluctuations and spin reorientation in hexagonal manganites. *J. Phys. Condens. Matter.* **2007**, *19*, 156228. [CrossRef]
20. Atou, T.; Chiba, H.; Ohoyama, K.; Yamaguchi, Y.; Syono, Y. Structure Determination of Ferromagnetic Perovskite $BiMnO_3$. *J. Solid State Chem.* **1999**, *145*, 639–642. [CrossRef]
21. Howard, C.J.; Campbell, B.J.; Stokes, H.T.; Carpenter, M.A.; Thomson, R.I. Crystal and magnetic structures of hexagonal $YMnO_3$. *Acta Cryst. B* **2013**, *69*, 534–540. [CrossRef] [PubMed]
22. Fiebig, M.; Fröhlich, D.; Kohn, K.; Leute, S.; Lottermoser, T.; Pavlov, V.V.; Pisarev, R.V. Determination of the Magnetic Symmetry of Hexagonal Manganites by Second Harmonic Generation. *Phys. Rev. Lett.* **2000**, *84*, 5620–5623. [CrossRef] [PubMed]
23. Holm, S.L.; Kreisel, A.; Schäffer, T.K.; Bakke, A.; Bertelsen, M.; Hansen, U.B.; Retuerto, M.; Larsen, J.; Prabhakaran, D.; Deen, P.P.; et al. Magnetic ground state and magnon-phonon interaction in multiferroic h-$YMnO_3$. *Phys. Rev. B* **2018**, *97*, 134304. [CrossRef]
24. Momma, K.; Izumi, F. *VESTA3* for three-dimensional visualization of crystal, volumetric and morphology data. *J. Appl. Cryst.* **2011**, *44*, 1272–1276. [CrossRef]
25. Skelton, E.F.; Webb, A.W.; Qadri, S.B.; Wolf, S.A.; Lacoe, R.C.; Feldman, J.L.; Elam, W.T.; Carpenter, E.R.; Huang, C.Y. Energy-dispersive X-ray diffraction with synchrotron radiation at cryogenic temperatures. *Rev. Sci. Instrum.* **1984**, *55*, 849–855. [CrossRef]
26. Bahl, C.; Andersen, P.; Klausen, S.; Lefmann, K. The monochromatic imaging mode of a RITA-type neutron spectrometer. *Nucl. Instr. Meth. B* **2004**, *226*, 667–681. [CrossRef]
27. Bahl, C.; Lefmann, K.; Abrahamsen, A.; Rønnow, H.; Saxild, F.; Jensen, T.; Udby, L.; Andersen, N.; Christensen, N.; Jakobsen, H.; et al. Inelastic neutron scattering experiments with the monochromatic imaging mode of the RITA-II spectrometer. *Nucl. Instrum. Methods Phys. Res. Sect. B Beam Interact. Mater. Atoms* **2006**, *246*, 452–462. [CrossRef]

28. Collins, M.F. *Magnetic Critical Scattering*; Oxford University Press: Oxford, UK, 1989.
29. Pailhès, S.; Fabrèges, X.; Régnault, L.P.; Pinsard-Godart, L.; Mirebeau, I.; Moussa, F.; Hennion, M.; Petit, S. Hybrid Goldstone modes in multiferroic $YMnO_3$ studied by polarized inelastic neutron scattering. *Phys. Rev. B* **2009**, *79*, 134409. [CrossRef]
30. Lovesey, S.W. *Theory of Neutron Scattering From Condensed Matter*; Polarization effects and magnetic scattering; Clarendon Press: Wotton-under-Edge, Gloucestershire, 1984; Volume 2.
31. Park, J.; Park, J.G.; Jeon, G.S.; Choi, H.Y.; Lee, C.; Jo, W.; Bewley, R.; McEwen, K.A.; Perring, T.G. Magnetic ordering and spin-liquid state of $YMnO_3$. *Phys. Rev. B* **2003**, *68*, 104426. [CrossRef]
32. Kadowaki, H.; Ubukoshi, K.; Hirakawa, K.; Martinez, J.L.; Shirane, G. Experimental study of new type phase transition in triangular lattice antiferromagnet VCl_2. *J. Phys. Soc. Jpn.* **1987**, *56*, 4027–4039. [CrossRef]
33. Kawamura, H. Universality of phase transitions of frustrated antiferromagnets. *J. Phys. Condens. Matter* **1998**, *10*, 4707. [CrossRef]
34. Gao, P.; Chen, Z.; Tyson, T.A.; Wu, T.; Ahn, K.H.; Liu, Z.; Tappero, R.; Kim, S.B.; Cheong, S.W. High-pressure structural stability of multiferroic hexagonal RMnO$_3$ (R = Y, Ho, Lu). *Phys. Rev. B* **2011**, *83*, 224113. [CrossRef]